

Boosting peracetic acid activation with Cu single-atom catalysts for sulfamethoxazole abatement: A nonradical pathway and ‘double engine’ driving mechanism

Longlong Zhang^{a,e}, Xuefei Zhou^{a,b,d}, Libin Yang^{a,*}, Yao Xu^a, Tongcai Liu^a, Ruicheng Ji^a, Yinchuan Yang^a, Yalei Zhang^{a,d}, Jiabin Chen^{a,c,d,**}

^a State Key Laboratory of Pollution Control and Resources Reuse, College of Environmental Science and Engineering, Tongji University, Shanghai 200092, China

^b Key Laboratory of Yangtze Water Environment for Ministry of Education, College of Environmental Science and Engineering, Tongji University, Shanghai 200092, China

^c Key Laboratory of Urban Water Supply, Water Saving and Water Environment Governance in the Yangtze River Delta of Ministry of Water Resources, College of Environmental Science and Engineering, Tongji University, Shanghai 200092, China

^d Shanghai Institute of Pollution Control and Ecological Security, Tongji University, Shanghai 200092, China

^e School of Safety and Environmental Engineering, Shandong University of Science and Technology, Qingdao 266590, China

ARTICLE INFO

Keywords:

Peracetic acid (PAA)
Cu single-atom catalyst
Singlet oxygenation
Emerging organic micropollutants
Double engine

ABSTRACT

Herein, a Cu single-atom catalyst with ultrahigh loading of Cu-pyridinic N₄ sites on carbon nanosheets (Cu_{SA}-N-C) is successfully designed and synthesized as an activator for peracetic acid (PAA). The Cu_{SA}-N-C showed the most powerful capacity for PAA activation among the Cu-based catalysts, and even a 48-fold enhancement on sulfamethoxazole (SMX) degradation compared to homogeneous Cu²⁺. The scavenging experiments and ESR analysis indicated that singlet oxygen (¹O₂) but not conventional radicals play a dominant role in SMX degradation. Theoretical calculations further insights into the generation of ¹O₂ in PAA activation. Furthermore, a ‘double engine’ driving mechanism was proposed, where the electron-rich area around Cu site and the electron-poor area around C site in the saturated Cu-N₄ configuration could efficiently adsorb and activate PAA. The Cu_{SA}-N-C/PAA process exhibited high tolerance towards the common water matrices (e.g., CO₃²⁻/HCO₃⁻ and Cl⁻), and thus showed excellent performance in the real wastewater. This study advances the understanding of non-radical PAA activation process and provides guidance for the design of smart PAA-active catalysts.

1. Introduction

Peracetic acid (PAA) is spotlighted as a green disinfectant, and increasingly used in the wastewater treatment owing to low risk of harmful byproducts formation [1]. Recently, PAA has emerged as a promising oxidant in degrading emerging organic micropollutants (EOMs) [2]. PAA can directly oxidize certain organic compounds (e.g., amino acids and β -lactam antibiotics) with electron-rich moieties, but suffers from high selectivity [3–5]. PAA has a weaker O–O bond (159 kJ/mol) than the commonly used peroxides, such as hydrogen peroxide (H₂O₂, 213 kJ/mol) and peroxymonosulfate (PMS, 317 kJ/mol) [6], implying the potential cleavage of the peroxide bond in PAA to generate powerful reactive species. The activation of PAA has

become an attractive way to achieve robust degradation of EOMs in wastewater treatment.

Various strategies have been developed to activate PAA for reactive species generation [2]. Among them, transition metals (e.g., Co, Fe and Cu) are regarded as highly prospective activators for PAA owing to their low cost and outstanding activation capacity [7–9]. Cu is a common metal ion, which plays an important role in the geochemical cycle and biological activities. Cu possesses unique Cu⁺/Cu²⁺/Cu³⁺ redox cycles, facilitating the catalytic reactions. Although Cu²⁺ ions showed much lower capacity for PAA activation than Co²⁺ and Fe²⁺ [10], the nano-CuO exhibited stronger catalytic activity for PAA than other nano-metal oxides including nano-Co₃O₄ and nano-Fe₂O₃ [11]. Copper-related catalysts with long-lasting activation capacity and low

* Corresponding author.

** Corresponding author at: State Key Laboratory of Pollution Control and Resources Reuse, College of Environmental Science and Engineering, Tongji University, Shanghai 200092, China.

E-mail addresses: neuyanglibin@126.com (L. Yang), chenjiabin@tongji.edu.cn (J. Chen).

<https://doi.org/10.1016/j.apcatb.2024.123897>

Received 3 January 2024; Received in revised form 19 February 2024; Accepted 27 February 2024

Available online 28 February 2024

0926-3373/© 2024 Elsevier B.V. All rights reserved.

toxicity have attracted increasing attention in PAA activation [12,13]. For example, it was reported that PAA could be catalyzed effectively by zero valent copper to produce hydroxyl radical ($\bullet\text{OH}$) and organic radicals ($\text{R-O}\bullet$) for diclofenac degradation [14]. Li et al. reported that the system of CuO-activated PAA significantly enhanced the inactivation of fungal spores in water [15]. In addition to using some oxides or other Cu species, the load of copper on the carbon material showed more excellent performance. Xiao et al. found that the formation of graphene shells on copper-based nanoparticles could strongly facilitated electron transfer from the core to the surface, facilitating the activation of PAA under neutral condition [12]. Yu et al. developed a carbon nitride hollow-nanotube catalysts with dispersed Cu(I) sites (Cu(I)-TCN) for the photocatalytic activation of PAA and achieved rapid removal of antibiotics [16]. In terms of EOMs degradation mechanism, the metal-activated PAA systems reported to date primarily depend on the generation of radical species, such as hydroxyl radical ($\bullet\text{OH}$) and organic radicals ($\text{R-O}\bullet$) [17]. However, these radical species are short lived and can be readily quenched by the complex water matrices (e.g., humic acid and carbonates) [18,19]. In this regard, restructuring PAA activation into a non-radical process is expected to be a more promising alternative, considering the resistance of non-radical oxidation to environmental interference [20]. On the other hand, the conventional copper-related nanoparticles are aggregated in water and suffer from low atomic utilization rates of surface metal sites, and fast release of metal ions. Therefore, there is an urgent need to develop new activators for PAA to achieve highly selective removal of EOMs from complex water matrices.

Single-atom catalysts (SACs) with metal atomically anchored on the support have become one of the most promising alternatives to abate metal pollution, maximize atomic utilization efficiency and achieve excellent catalytic activity [21,22]. The most important feature of SACs is the isolated distribution of metal active centers at the atomic level on the substrate [23]. This approach not only maximizes the atomic utilization efficiency of metal species, but also creates the well-defined and standardized coordination structure, favoring deeper insight into the catalytic mechanisms at the atomic level [24]. Moreover, the strong covalent binding between the metal centers and the supports enables SACs superior structural robustness and stability over their nanoparticle counterparts, significantly restricting the leaching of metal ions [25]. Recently, the SACs with metal loaded onto N-functionalized carbon material (named M–N–C SACs, M = Fe, Co, Cu, etc.) demonstrated remarkable performance in Fenton-like catalysis, in terms of efficiency and durability [26]. Li et al. synthesized a single-atom Cu catalyst with the unsaturated Cu–N₂ configuration to activate peroxydisulfate (PDS), which exhibited an obvious selective and anti-interference performance for pollutant degradation in a complex matrix due to the generation of Cu(III) [27]. Lu et al. found that the oxidation of singlet oxygen ($^1\text{O}_2$) and electron transfer process induced by a single-atom Cu catalyst with saturated Cu–N₄ sites in the activation of peroxymonosulfate (PMS) dominated the degradation of pollutants [28]. Obviously, the mechanism of Cu–N–C SACs for peroxide oxidants (e.g., PDS, PMS, PAA) activation is very complex and closely related to the coordination structure of the SACs. Although Cu–N–C SACs appear to be an ideal activator candidate for PAA, the related study remains largely absent, and further efforts are required to reveal the underlying catalytic mechanism.

In this work, a Cu–N–C SAC with Cu sites atomically anchored on ultrathin nitrogen-doped carbon nanosheets (Cu_{SA}–N–C) was successfully fabricated and further employed for PAA activation. The rational design and synthesis of Cu_{SA}–N–C delivers a high single atomic Cu loading over most catalysts reported so far. The single-atomic structure and electronic properties of Cu_{SA}–N–C were comprehensively analyzed using various characterization techniques, e.g., X-ray absorption spectroscopy (XAS). The Cu_{SA}–N–C exhibits significantly stronger capacity on PAA activation than its homogeneous and nanoparticle counterparts (Cu²⁺ and nCuO). Interestingly, a unique non-radical pathway in PAA activation with

Cu_{SA}–N–C was uncovered, which is largely distinct from the radical process in the conventional PAA activations. By a combined experimental and density functional theory (DFT) investigation, the origin of high-activity of the Cu_{SA}–N–C catalyst towards PAA activation was unraveled. To the best of our knowledge, this study is among the first to introduce the single-atom catalysts for efficient PAA activation, and unveil the significance of non-radical oxidation in PAA-based AOPs. This work can help to bridge the knowledge gap of PAA activation process and inspire the design of highly active catalyst for wastewater treatment.

2. Materials and methods

2.1. Chemicals

The source of the reagents used in this experiment is provided in the [Supporting Information](#) (SI, Text S1). The real water samples were obtained in Huangpu River and local sewage plant as the representative surface water and wastewater, respectively, with the water quality parameters provided in the SI ([Table S1](#)).

2.2. Synthesis and characterizations of Cu_{SA}–N–C

2.2.1. Synthesis procedure

In a typical synthetic procedure, the mixture of 10.5 mmol of Cu (CO₂CH₃)₂·H₂O and 5.25 mmol of L-glutamic acid were dissolved in 500 ml of deionized water. 1,3,5-benzenetricarboxylic acid (5.52 mmol) was dissolved in a mixed solution containing 450 ml of deionized water and 50 ml of ethanol, which was subsequently added into the above-obtained solution with stirring. After 2 h of stirring at ambient environment, the resulting blue precipitates were collected by filtration, washed thoroughly with water, and finally dried under vacuum at 50 °C for 24 h. The obtained sky-blue powders were denoted as Cu–C precursor.

After that, the precursor and dicyandiamide were mixed at a mass ratio of 1:10 by grinding in a mortar, followed by pyrolysis at 800 °C with a ramping rate of 3 °C min^{−1} and kept for 180 min under argon atmosphere. After natural cooling down to room temperature, the black powders were further soaked in oxygen saturated HCl (5% aq.) for 4 h to remove surface adsorbed and weakly bound metal residues, devoted as Cu_{SA}–N–C. The Cu–C control sample was synthesized under the same conditions except with absence of dicyandiamide. The N–C composite was obtained under the same conditions as Cu_{SA}–N–C except replacing of the Cu–C precursor with trimesic acid.

2.2.2. Characterizations of the catalyst

Aberration corrected high-angle annular dark-field scanning TEM (HAADF-STEM) characterization was conducted on JEOL JEM-ARM300F STEM/TEM to visualize the single-atom structure. The X-ray absorption spectroscopy (XAS) measurements for the Cu-edge were conducted in transmission mode (fluorescence mode) on beamline 12-BM in the Advanced Photon Source at Argonne National Laboratory. X-ray absorption near-edge structure (XANES) and extended X-ray absorption fine structure (EXAFS) data reduction and analysis were analyzed by Athena and Artemis software. Copper phthalocyanine (CuPc) and copper phthalocyanine (CuPc) were used as references. The morphology and elements distribution of the catalysts were characterized by scanning electron microscopy (SEM, JSM 7800 F) equipped with energy dispersive X-ray spectroscopy (EDXS) and high-resolution transmission electron microscopy (HRTEM, JEM-2100). X-ray photoelectron spectroscopy (XPS) was collected on a Thermo Fisher Scientific ESCALAB 250XI system with the C 1 s peak (284.6 eV) as reference. The metal loading of Cu_{SA}–N–C was quantified by inductively coupled plasma optical emission spectroscopy (ICP-OES, Agilent 5110, USA) detection. The content of the leaching Cu was measured on inductively coupled plasma-mass spectrometry (ICP-MS) on an Optima 7300 DV (Perkin-Elmer Corporation).

2.3. Experimental procedures

To evaluate the catalytic activity of $\text{Cu}_{\text{SA}}\text{-N-C}$ for PAA, sulfamethoxazole (SMX) was selected as a model pollutant. In a typical experiment, 100 ml of 10 μM SMX solution was mixed with 20 mg of the catalyst and magnetically stirred for 20 min to achieve adsorption-desorption equilibrium. The reaction was triggered by dosing 0.52 mM of PAA solution, and the initial pH was then immediately adjusted to 7.0 using NaOH (0.2 M) and H_2SO_4 (0.1 M). The samples (1.0 ml) were withdrawn at predetermined time intervals and immediately quenched with excess NaS_2O_3 (10 mM) prior to analysis. The reusability of $\text{Cu}_{\text{SA}}\text{-N-C}$ was tested by the cycling experiment. After each run, the catalyst was recovered by filtration, washed thoroughly with deionized water and then reused after vacuum drying.

2.4. Chemical analysis

The analytical methods of target organics are illustrated in the SI (Text S2). The detailed information of the HPLC analytical methods for the target organics are summarized in the SI (Table S2). Theoretical and

computational details are also shown in the SI (Text S3).

3. Results and discussion

3.1. Synthesis and characterizations of $\text{Cu}_{\text{SA}}\text{-N-C}$

The typical synthesis procedure of $\text{Cu}_{\text{SA}}\text{-N-C}$ is shown in Fig. 1a. A nitrogen-free Cu metal-organic framework (MOF) was primarily obtained as the precursor. Subsequently, the Cu precursor was mixed with dicyandiamide, engaging as a nitrogen source, followed by the thermal treatment under argon atmosphere to produce the $\text{Cu}_{\text{SA}}\text{-N-C}$ material. The introduction of dicyandiamide is crucial to securely trap copper atoms and avoid their agglomeration during the calcination. The SEM (Fig. 1b) and TEM images (Fig. 1c) show that $\text{Cu}_{\text{SA}}\text{-N-C}$ exhibited a two-dimensional ultra-thin nanosheet structure as the N-C material (Fig. S1). Without dosing dicyandiamide, the Cu-C material formed a porous carbon cube inside with abundant copper microspheres (Fig. S2), indicating the indispensable role of dicyandiamide in the formation of $\text{Cu}_{\text{SA}}\text{-N-C}$ sheet morphology. As observed from the lattice fringe picture in Fig. 1d, the $\text{Cu}_{\text{SA}}\text{-N-C}$ surface consisted of abundant N-C fused layers.

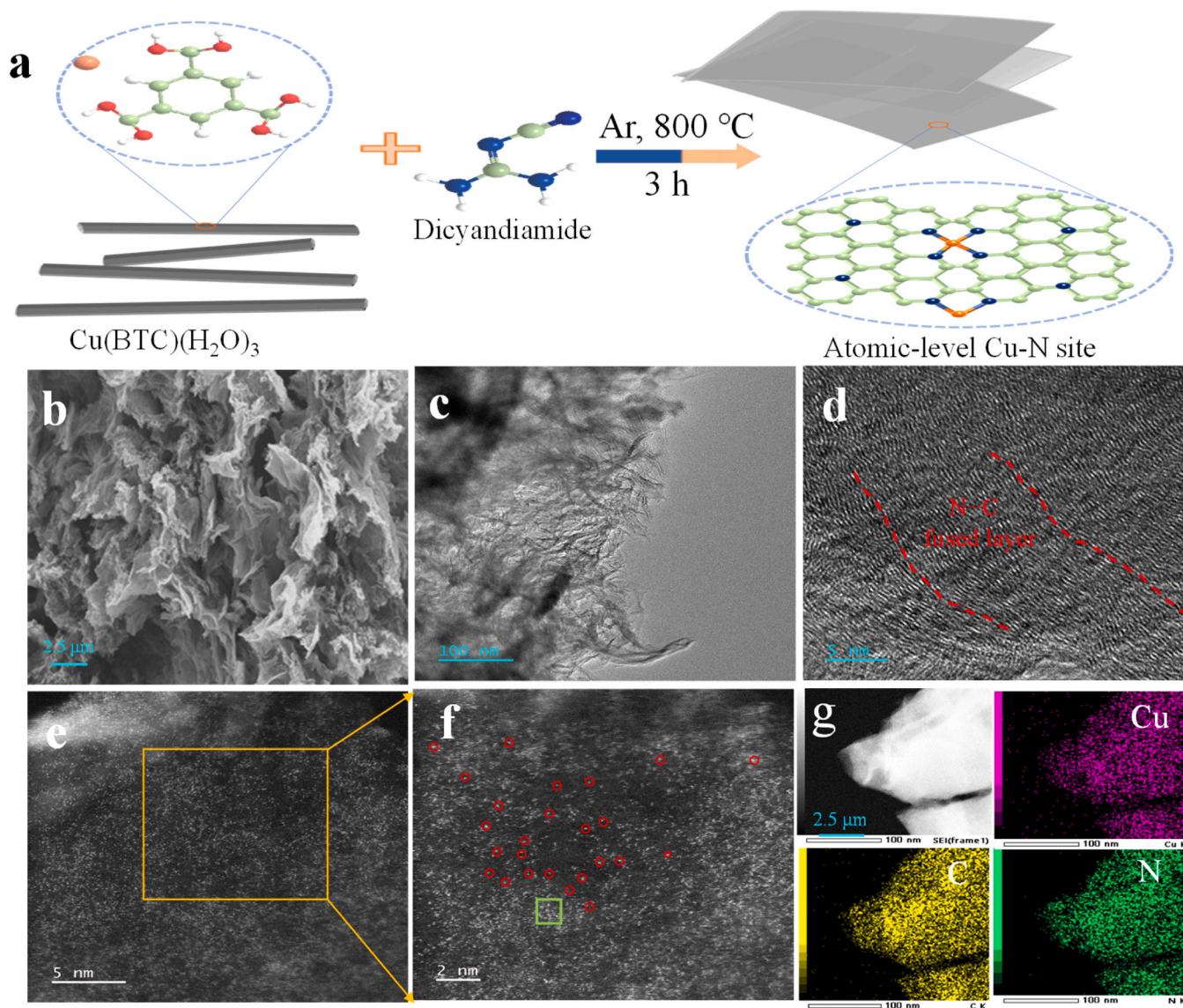


Fig. 1. (a) Schematic illustration of the synthesis of $\text{Cu}_{\text{SA}}\text{-N-C}$; (b) SEM, (c) TEM, (d) Fig. S1. (a) SEM image, (b) TEM image and (c) high-resolution transmission electron microscopy (HRTEM) image, (e, f) high-angle annular dark-field scanning transmission electron microscopy (HAADF-STEM) image, and (g) energy-dispersive X-ray (EDX) mappings of the $\text{Cu}_{\text{SA}}\text{-N-C}$ sample.

The spherical aberration-corrected HAADF-STEM was further conducted to determine the dispersed state of Cu atoms. As Figs. 1e and 1f shows, numerous small bright dots (partly highlighted by yellow circles) clearly appeared in HAADF-STEM image of Cu_{SA}-N-C, while nanoclusters or sub-nanoparticles were not observed. This result indicates the enrichment of the atomically dispersed Cu atoms in N-C sheet. The associated EDX elemental mapping confirmed the homogeneous distribution of Cu, C and N in the N-C fused layer (Fig. 1g). A high loading of single atomic Cu up to 20.3 wt% in Cu_{SA}-N-C was detected with ICP-OES, agreeing well with the EDX result (19.8 wt%). The BET surface area in Fig. S3a collectively indicated approximate 9.6 atoms per nm² of Cu loading on Cu_{SA}-N-C surface (as highlighted via the green square in Fig. 1f). Like the N-C sample, a broad peak centered at around 26.7° emerged in the XRD pattern of Cu_{SA}-N-C (Fig. S3b), corresponding to the graphitic carbon layer. Moreover, the peaks of metallic Cu or Cu oxide are not observed in XRD pattern of Cu_{SA}-N-C sample. The full-scan spectrum of XPS in Fig. S4a shows that Cu, N and C are the dominant components in Cu_{SA}-N-C with the atomic percentage contents of 3.1%, 15.7% and 81.2%, respectively. Two major signals at 934.6 and 932.4 eV emerged in the high-resolution Cu 2p spectrum of Cu_{SA}-N-C (Fig. S4b), suggesting the presence of Cu(II) and Cu(I), respectively [11]. Three peaks are centered at 398.6, 400.8 and 403.7 eV in the high-resolution N 1s spectrum (Fig. S4c), assigning to pyridinic N (62.3%), graphitic N (30.5%) and oxidized N species (7.2%), respectively [29,30]. The pyridinic N is generally considered as the coordinating sites for transition metals [31], thus high abundance of pyridinic N is favorable for coordination of single-atom Cu.

The local structure and coordination environment of Cu species at atomic level in Cu_{SA}-N-C were further characterized by X-ray absorption spectroscopy (XAS). Fig. 2a shows the Cu K-edge X-ray absorption near-edge structure (XANES) spectra of Cu_{SA}-N-C using Cu foil and copper phthalocyanine (CuPc) as references. The absorption edge position of

Cu_{SA}-N-C was located between those of Cu foil and CuPc, indicating that the valence state of Cu is between 0 and +2. In the Fourier transform (FT) k^3 -weighted Cu K-edge EXAFS curve (Fig. 2b), the Cu_{SA}-N-C exhibited a predominant peak at approximate 1.5 Å, which was attributed to the Cu–N coordination. The peak at around 2.2 Å, characteristic of Cu–Cu coordination, was not observed in the EXAFS, indicating the absence of Cu nanoclusters or nanoparticles in Cu_{SA}-N-C. These results can be further confirmed by the wavelet transforms (WT) of EXAFS plots, which can distinguish the backscattering atoms and provide the R-space condition. As shown in Fig. 2e, the WT analysis showed that Cu_{SA}-N-C possessed a well-defined Cu–N₄ coordinated sites identical to CuPc, further revealing the atomic dispersion of Cu in Cu_{SA}-N-C. The Cu K-edge EXAFS fitting was conducted to investigate the quantitative structural parameters of the Cu atoms in Cu_{SA}-N-C. As Fig. 2c shows, the EXAFS spectra can be well fitted by the proposed Cu–N₄ structure, and the coordination number of Cu–N was calculated to be 3.85 in average with a bond length of 1.95 (Table S3). The results indicated that the isolated Cu atom in Cu_{SA}-N-C was mostly coordinated with four N atoms. Besides, DFT calculations were employed to provide in-depth insight into the coordination mode of Cu–N in Cu_{SA}-N-C. The coordination of Cu with pyridinic N or pyrrolic N in the constructed monolayer graphene model were considered in the calculation. As illustrated in Fig. 2d, the formation energy (E_f) required for the Cu–pyridinic N₄ construction was significantly lower than that of the Cu–pyrrolic N₂ configuration, suggesting that an isolated Cu atom tends to coordinate with pyridine N in a tetra-ligand configuration, i.e., Cu–pyridinic N₄. Overall, the above analysis strongly evidenced the atomic dispersion of Cu atoms coordinated by four pyridinic N atoms in the Cu_{SA}-N-C.

3.2. PAA activation with Cu_{SA}-N-C for efficient contaminant degradation

As shown in Fig. 3a, SMX was slightly removed by Cu_{SA}-N-C or PAA

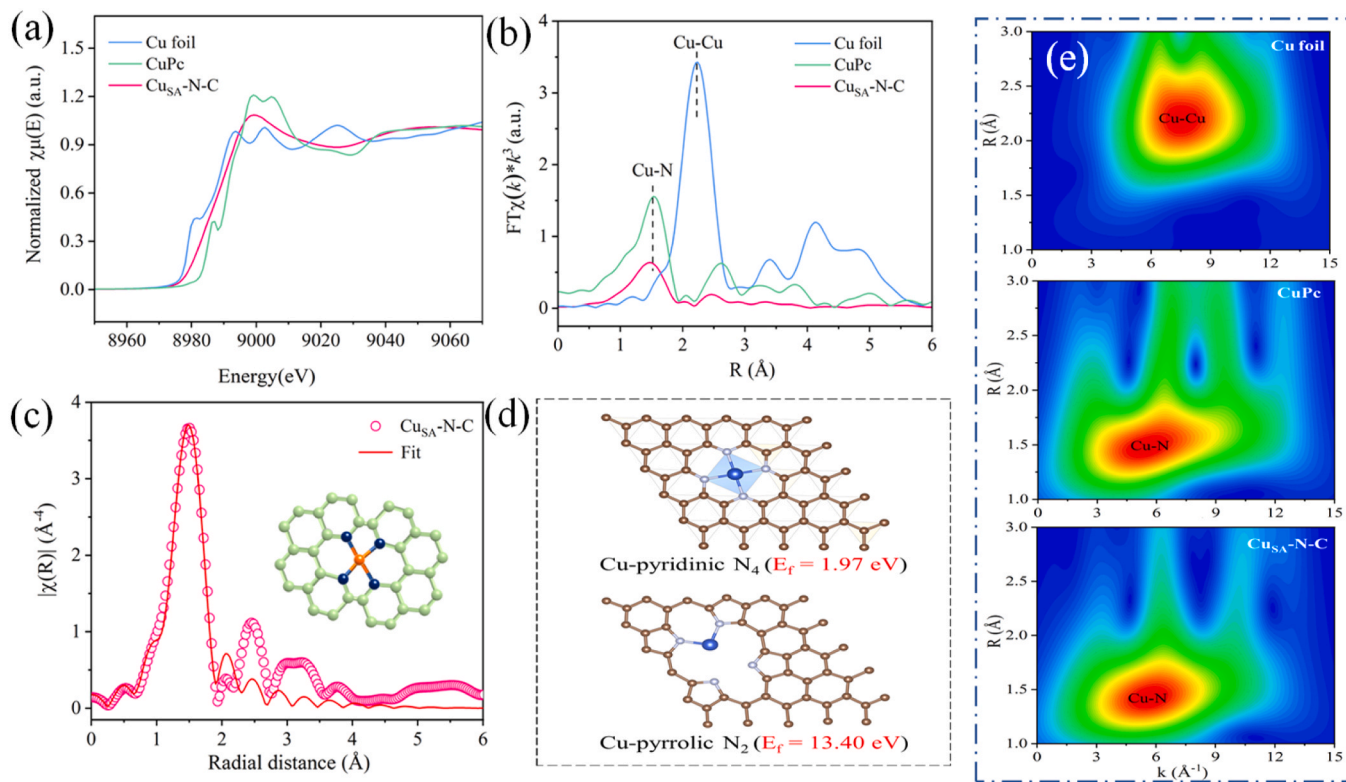


Fig. 2. (a) X-ray absorption near-edge structure (XANES) spectra, (b) Fourier transform extended X-ray absorption fine structure (FT-EXAFS) spectra of Cu_{SA}-N-C and the reference samples and (c) corresponding FT-EXAFS fitting curve at R space of the Cu_{SA}-N-C sample (inset: molecular model of CuN₄ site on the Cu_{SA}-N-C sample); (d) Atomic structure models and the calculated formation energies (E_f) of Cu–pyridinic N₄ and Cu–pyrrolic N₂ configurations for the Cu_{SA}-N-C, including C (gray), N (white), and Cu (blue) atoms; (e) wavelet transforms for the k^2 -weighted EXAFS signals of Cu_{SA}-N-C and the reference samples.

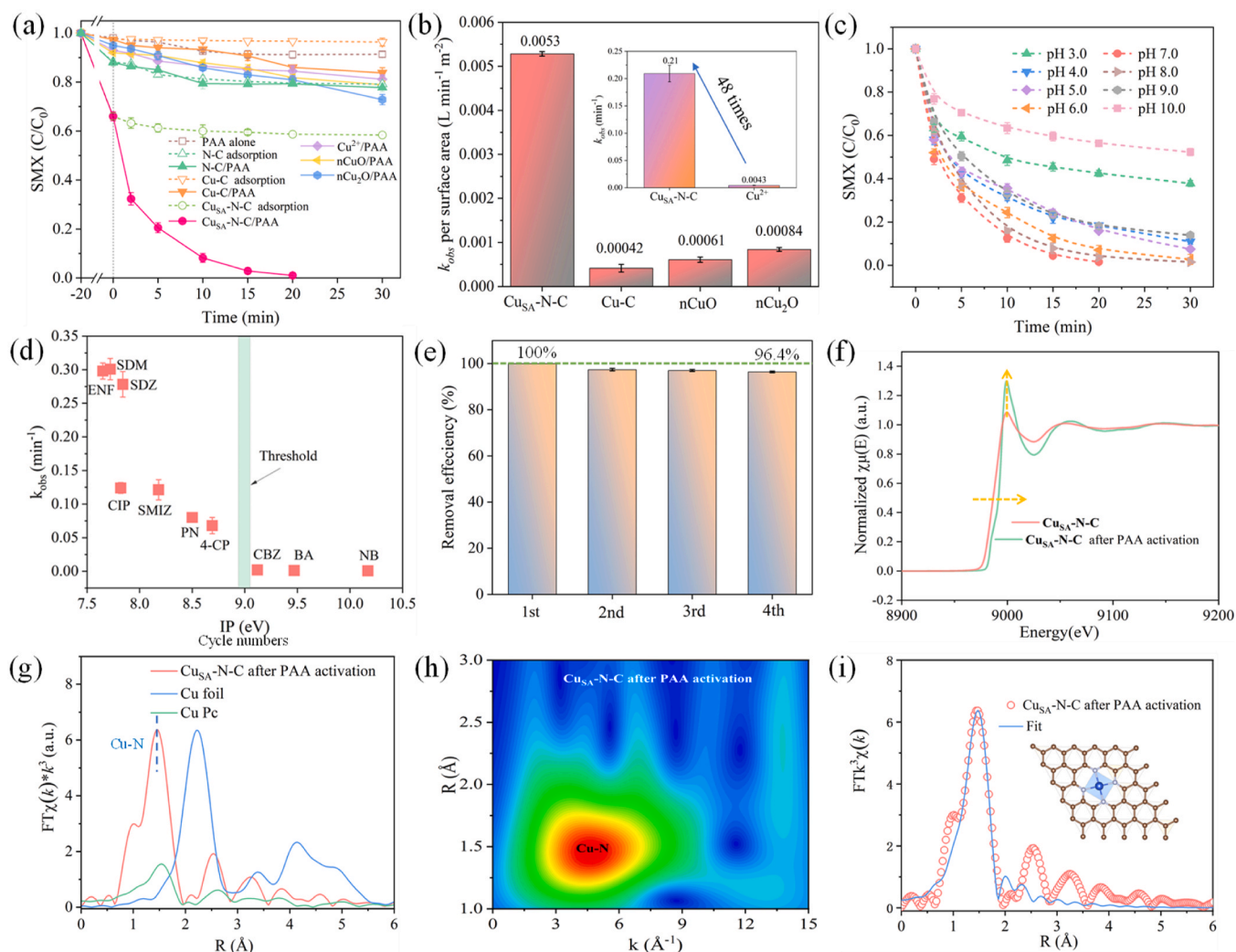


Fig. 3. (a) Kinetics of SMX degradation by PAA activated with $\text{Cu}_{\text{SA}}\text{-N-C}$ other control samples; (b) Specific activity comparisons of $\text{Cu}_{\text{SA}}\text{-N-C}$ and other Cu-related catalysts (b insert was the comparison of $\text{Cu}_{\text{SA}}\text{-N-C}$ and Cu^{2+} on reaction rate constants); (c) effects of initial pHs on the degradation of SMX in the $\text{Cu}_{\text{SA}}\text{-N-C/PAA}$ process; (d) the relationships between the k_{obs} of different organic pollutants and their ionization potential (IP) value; (e) degradations of SMX in the $\text{Cu}_{\text{SA}}\text{-N-C/PAA}$ process during continuous cycles; (f) normalized Cu K-edge XANES of the $\text{Cu}_{\text{SA}}\text{-N-C}$ before and after reaction, (g) FT of Cu K-edge EXAFS spectra, (h) the wavelet transforms for the k_2 -weighted EXAFS signals and (i) FT-EXAFS fitting curve of the $\text{Cu}_{\text{SA}}\text{-N-C}$ at R space of the $\text{Cu}_{\text{SA}}\text{-N-C}$ after reacting with PAA. Reaction conditions: catalyst dosage = 0.2 g/L, $[\text{PAA}]_0 = 0.52$ mM, $[\text{contaminants}]_0 = 10$ μM , $\text{pH}_0 = 7.0$ if not otherwise specified.

alone, but could be completely degraded within 20 min by the coupling of $\text{Cu}_{\text{SA}}\text{-N-C}$ and PAA. Meanwhile, the rapid decomposition of PAA was observed with $\text{Cu}_{\text{SA}}\text{-N-C}$ (Fig. S5), suggesting that $\text{Cu}_{\text{SA}}\text{-N-C}$ was effective to activate PAA to generate reactive species. Noting that Cu-C or N-C was inefficient to activate PAA to degrade SMX, the single atomic Cu sites coordinated with pyridinic N in $\text{Cu}_{\text{SA}}\text{-N-C}$ was assumed as the active sites for PAA activation. The degradation rate constant (k_{obs}) of SMX by $\text{Cu}_{\text{SA}}\text{-N-C/PAA}$ process was 48 times higher than that of the homogeneous counterpart of $\text{Cu}^{2+}/\text{PAA}$ process (Fig. 2b insert), further suggesting the effectiveness of PAA activation by heterogeneous Cu active sites. The k_{obs} of SMX was further normalized by the surface area (Table S4) and catalyst dosage (denoted as nk_{obs}), i.e., the rate constant per surface area, to compare the intrinsic catalytic activity of the catalysts in various Cu heterogeneous activation systems. As shown in Fig. 2b, the nk_{obs} of SMX in the $\text{Cu}_{\text{SA}}\text{-N-C/PAA}$ system is 12.6, 8.7 and 6.3 times higher than those of PAA activated by Cu-C, nano-CuO (nCuO), and nano-Cu₂O (nCu₂O), respectively, suggesting the excellent performance of single atomic Cu sites on PAA activation. Besides, the contribution of the co-existing H_2O_2 in PAA solution could be ruled out, because SMX was hardly degraded by $\text{H}_2\text{O}_2/\text{Cu}_{\text{SA}}\text{-N-C}$ (Fig. S6).

The degradation of SMX was rapid at near-neutral pH conditions, but

was significantly slow down at strong acidic or alkaline pHs (Fig. 3c). To be specific, SMX was almost completely removed with the corresponding k_{obs} being 0.12–0.21 min^{-1} at pH 5.0–8.0 (Fig. S7). Nevertheless, the k_{obs} markedly decreased to approximate 0.026 and 0.018 min^{-1} at pH 3.0 and pH 10.0, respectively. PAA has a pK_a of around 8.2, and thus the conjugate acid of PAA (PAAH) is predominant at pH 3.0. Based on the DFT calculation, the optimized structure of PAAH has a shorter O–O bond length than that of the anionic species of PAA (PAA^-) (Fig. S8), suggesting that PAAH was more difficult activation than PAA^- . Moreover, PAA is positively charged at strong acid conditions due to the H-bond formed between H^+ and PAA; while $\text{Cu}_{\text{SA}}\text{-N-C}$ surface is positively charged at pH 3.0 owing to its isoelectric point (pH_{IEP}) of pH 4.2 (Fig. S9). Hence, the strong acidic pH was unfavorable for the interaction between PAA and $\text{Cu}_{\text{SA}}\text{-N-C}$ owing to the electrostatic repulsion, and thus $\text{Cu}_{\text{SA}}\text{-N-C}$ was inefficient to activate PAA for SMX degradation at pH 3.0. Under strong alkaline condition (i.e., pH 10.0), most of PAA ($> 99\%$) would be dissociated to form PAA^- . Hence, the interactions between PAA^- and negatively charged $\text{Cu}_{\text{SA}}\text{-N-C}$ surface would be obstructed at pH 10.0 due to the electrostatic repulsion. Though PAA^- is more susceptible to activation due to the longer O–O bond, the hydrolysis of PAA becomes much stronger at strong alkaline pHs. Hence,

PAA was quickly consumed at pH 10.0 (Fig. S5), and thus the oxidation of SMX was significantly inhibited.

The degradation of various organic contaminants by the Cu_{SA}-N-C/PAA process was also examined. As Fig. S10 shows, the degradation of the five antibiotics (i.e., ciprofloxacin (CIP), enrofloxacin (ENF), sulfadiazine (SDZ), sulfadimoxine (SDM) and sulfamethizol (SMIZ)) were higher than that of phenol (PN) and 4-chlorophenol (4-CP) in the Cu_{SA}-N-C/PAA system, and the degradation of nitrobenzene (NB), benzoic acid (BA) and carbamazepine (CBZ) could be neglected. The correlation between the degradation rates and ionization potential (IP), a commonly used molecular descriptors, is further established to reveal the structural selectivity of contaminant oxidation in the Cu_{SA}-N-C/PAA system. IP reflects the energy difference between the positively charged molecule and the neutral one in the same molecular geometry [32]. The electron-donating moieties (e.g., hydroxyl and amine) can lower the IP value of the organics, while the electron-withdrawing groups (e.g., carboxyl and nitril) has the opposite effect [33]. Obviously, the organics (CIP, ENF, SMIZ, SDZ, SDM, PN and 4-CP) with lower IP values (< 9.0 eV, the supposed threshold) were vulnerable to oxidation, while those (NB, BA and CBZ) possessing higher IP values could be barely degraded in the Cu_{SA}-N-C/PAA process (Fig. 3d). This result was quite different from the radical-dominated processes [18], but resembled some non-radical (e.g., ¹O₂, Fe(IV) and Co(IV)) processes [34–36]. Hence, the contaminant degradation might not be contributed from the radicals, but from the non-radical oxidizing species.

The Cu_{SA}-N-C exhibited a superior durability in PAA activation with SMX degradation marginally reduced by 3.6% after four consecutive cycles (Fig. 3e). The leaching of Cu²⁺ during the cycle tests were only 70 ~ 83 μg L⁻¹ (Fig. S11a), which was much lower than the permissible limit of Cu (1 mg L⁻¹) based on the drinking water quality standard in China (GB 5749–2006). It is worthwhile mentioning that Cu²⁺ in the maximum leaching content (83 μg L⁻¹) showed negligible effect on SMX removal by PAA (Fig. S11b). Hence, the activation of PAA was dominantly induced by heterogeneous catalytic reaction on the Cu_{SA}-N-C. The XRD pattern of Cu_{SA}-N-C after reacting with PAA was identical to the pristine one (Fig. S3b), suggesting the stability of the catalyst's crystalline structure and absence of Cu species aggregating on the N-C surface after reaction. Meanwhile, the N 1s and Cu 2p_{3/2} XPS analysis revealed that the fractions of N species (pyridinic N, graphitic N and oxidized N) and Cu species (Cu(II) and Cu(I)) in the used Cu_{SA}-N-C remain extremely close to the raw material (Fig. S12), reflecting the stability of the chemical structure. The dispersed state and coordination environment of Cu atoms in Cu_{SA}-N-C after reacting with PAA was further investigated by HADDF-STEM and XAS analyses. From Fig. S13, large amounts of atomically dispersed Cu sites were still observed in the HADDF-STEM image of the reacted Cu_{SA}-N-C, showing no visible change compared to the original sample. The Cu K-edge XANES spectrum of Cu_{SA}-N-C after reaction exhibited a slight enhancement of the intensity of the major absorption peak and a positive shift toward higher energy for the pre-edge centroid (Fig. 3f), which might be attributed to the formation of other coordination bonds on the Cu-pyridinic N₄ site [37]. The R space of Cu K-edge XANES spectrum (Fig. 3g) and WT map of EXAFS plots (Fig. 3h) showed that only Cu–N coordination existed in the reacted Cu_{SA}-N-C, while no obvious metallic Cu–Cu bond was detected. Hence, Cu was still atomically dispersed in the Cu_{SA}-N-C after the reaction. Further, the average Cu–N coordination number of Cu was calculated to be 3.88 for Cu_{SA}-N-C after PAA activation (Fig. 3i, Table S5), indicating the preservation of Cu–N₄ configuration in the Cu_{SA}-N-C after reaction. Overall, the above evidences strongly demonstrated the high stability of Cu_{SA}-N-C during PAA activation.

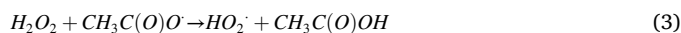
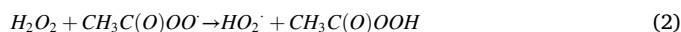
3.3. Identification of reactive species in the Cu_{SA}-N-C/PAA system

3.3.1. Nonradical vs radical process

Generally, the activation of PAA can generate [•]OH, R–O[•] (including [•]CH₃, CH₃O[•], CH₃CO[•] and CH₃CO₂[•]) and hydroperoxyl

radicals/superoxide radical anion (HO₂[•]/O₂^{•-}) as the reactive species [38]. EPR analyses with DIPPMPO as the spin trapping agent were conducted to reveal the generation of [•]OH and R–O[•] in the Cu_{SA}-N-C/PAA system, and the simulation of EPR spectrum was further performed to distinguish the radical capture products. The obtained hyperfine splitting constants (a_p, a_N, and a_H) (Table S6) and simulated EPR curve (Fig. 4a, Fig. S14) indicated the existence of [•]OH, [•]CH₃, CH₃O[•] and CH₃CO[•]. Noting that the characteristic peaks of DIPPMPO–[•]OH and DIPPMPO–(R–O[•]) adducts were not observed in PAA solution, but clearly appeared after addition of Cu_{SA}-N-C (Fig. S15), these radicals were generated from the activation of PAA by Cu_{SA}-N-C. Scavenging experiments were further conducted to evaluate the contribution of [•]OH and R–O[•] on SMX degradation in the Cu_{SA}-N-C/PAA process. Tert-butanol (TBA) can rapidly react with [•]OH (k_{app} = 4.0 × 10⁸ L·mol⁻¹·s⁻¹), but was inert for R–O[•], while methanol (MeOH) reacts readily with both [•]OH and R–O[•] [39]. The presence of TBA showed negligible effect on SMX degradation (Fig. 4d), indicating that [•]OH contributed less to SMX degradation. The addition of MeOH also slightly inhibited the degradation of SMX, and hence, R–O[•] might not be the major reactive species.

Literature has shown that 2,4-hexanedione (2,4-HD) can be a suitable quencher for R–O[•] [8]. 2,4-HD addition had little impact on the degradation of SMX, evidencing that R–O[•] played a little role in SMX degradation. This phenomenon was largely different from the conventional metal-activated PAA systems, in which [•]OH and R–O[•] were dominantly generated as the primary reactive species [2]. Besides, HO₂[•]/O₂^{•-} can be formed in PAA-based AOPs through the unimolecular decay of CH₃CO[•] (k = 1.82 s⁻¹, Eq. 1) [40] and the reaction of H₂O₂ with CH₃CO[•] (Eq. 2), CH₃CO[•] (Eq. 3) or [•]OH (Eq. 4) [41]. EPR detection reveals the generation of HO₂[•]/O₂^{•-} with PAA activated by Cu_{SA}-N-C (Fig. 4b). Meanwhile, the degradation of SMX was moderately inhibited after addition of 10 mM *p*-benzoquinone (*p*-BQ) (Fig. 4d), an efficient scavenger for HO₂[•]/O₂^{•-} (k_{app} = 0.9–1 × 10⁹ M⁻¹s⁻¹) [42], suggesting that HO₂[•]/O₂^{•-} might be involved in SMX oxidation. However, HO₂[•]/O₂^{•-} generally has a low oxidative reactivity towards organic contaminants due to its weak oxidation capacity (E_{h0} = 0.33 V). As shown in Fig. 4b, the peak intensity of DMPO–HO₂[•]/O₂^{•-} signal in EPR spectrum was not reduced after dosing SMX, excluding the direct contribution of HO₂[•]/O₂^{•-} for SMX oxidation. Hence, HO₂[•]/O₂^{•-} was not directly responsible for SMX degradation, but might act as a significant intermediate for reactive species generation.



The afore-mentioned results indicated that the oxidation of SMX in the Cu_{SA}-N-C/PAA process was not attributed to the widely reported radical species in PAA-based AOPs; instead, a non-radical oxidation process might be the dominant mechanism. Singlet oxygen (¹O₂) can be generated via the attack on central C atom of PAA by peroxy-group, while this reaction is too weak to allow the efficient production of ¹O₂. Herein, the typical signal assigning to TEMP-¹O₂ adduct was clearly observed in the Cu_{SA}-N-C/PAA system, but not occurred with PAA or Cu_{SA}-N-C alone (Fig. 4c), indicating the production of ¹O₂ after PAA activation by Cu_{SA}-N-C. L-histidine and furfuryl alcohol (FFA) are the typical ¹O₂ scavengers with the rate constants of 3.2 × 10⁷ and 1.2 × 10⁸ M⁻¹ s⁻¹, respectively [43]. As Fig. 4d shows, the oxidation of SMX was significantly suppressed in the presence of L-histidine or FFA, while PAA decomposition was barely affected (Fig. 4e). It is thus suggested that the inhibition of SMX degradation was attributed to the scavenging of ¹O₂, but not the consumption of PAA. Hence, ¹O₂ might be the major reactive species for SMX degradation. Moreover, the EPR intensity of ¹O₂ signal

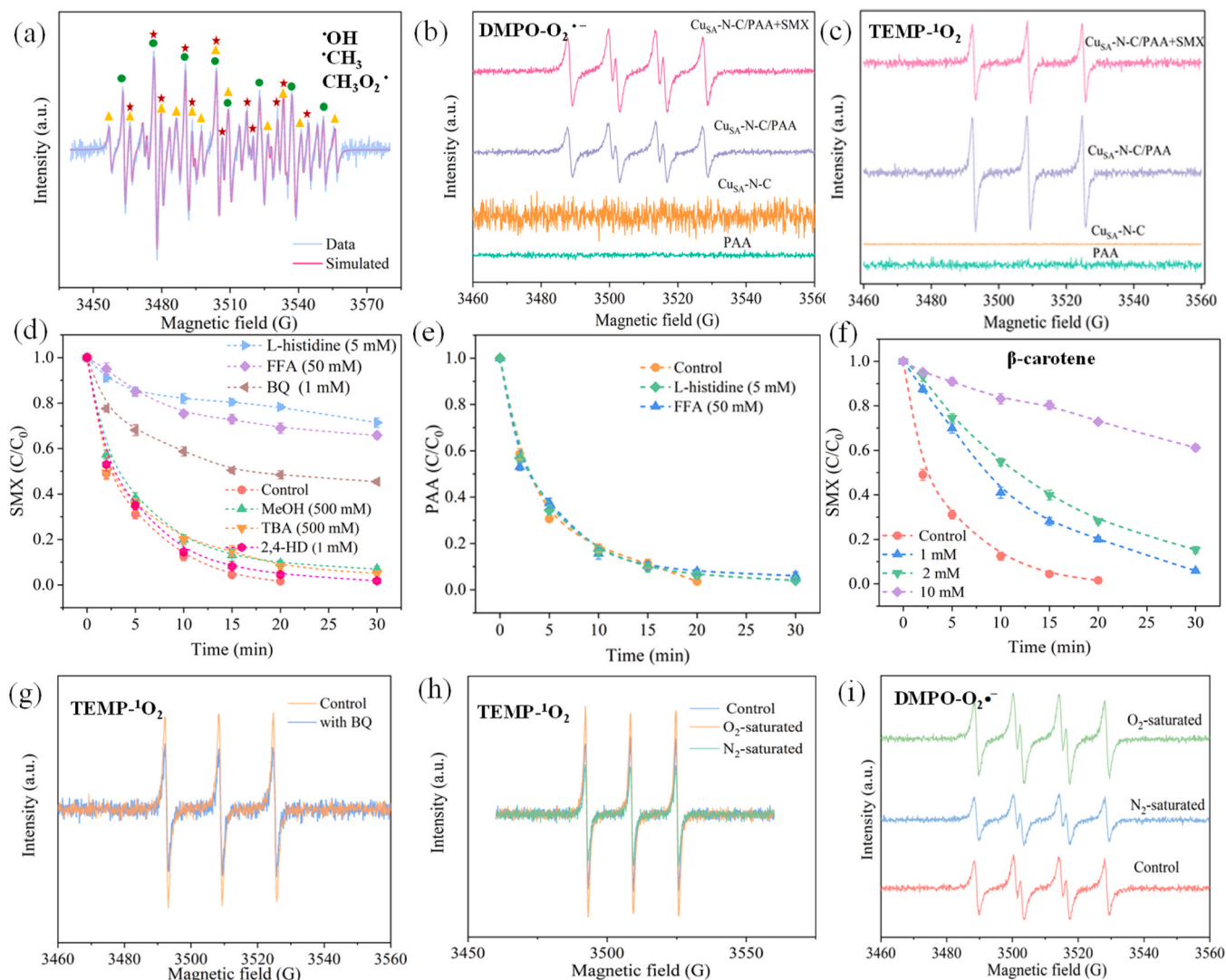


Fig. 4. (a) Experimental and simulated EPR spectra of spin-trap adducts using DIPPMPO as the trapping agents for $\bullet\text{OH}$ and $\text{R-O}\bullet$; EPR spectra with (b) DMPO in methanol and (c) TEMP in different systems; kinetics of (d) SMX degradation and (e) PAA decomposition with and without the presence of different quenchers; (f) effects of β -carotene on SMX degradation. Reaction conditions: catalyst dosage = 0.2 g/L, $[\text{PAA}]_0 = 0.52 \text{ mM}$, $[\text{SMX}]_0 = 10 \text{ }\mu\text{M}$, $\text{pH}_0 = 7.0$. (g) Effects of benzoquinone (BQ) on the generation of $\text{TEMP-}^1\text{O}_2$ adduct; (h) $\text{TEMP-}^1\text{O}_2$ adduct and (i) $\text{DMPO-O}_2^{\bullet-}$ adduct formed in the $\text{Cu}_{\text{SA}}\text{-N-C/PAA}$ process under ambient, N_2 -saturated and O_2 -saturated conditions.

apparently decreased once SMX was dosed (Fig. 4b), directly reflecting the contribution of $^1\text{O}_2$ to SMX oxidation. To further unveil the importance of $^1\text{O}_2$ in the $\text{Cu}_{\text{SA}}\text{-N-C/PAA}$ process, SMX degradation was evaluated in the presence of β -carotene, which has a high reaction rate constant with $^1\text{O}_2$ ($k_{\text{app}} = 2 \sim 3 \times 10^{10} \text{ M}^{-1} \text{ s}^{-1}$) [44], but was inert to PAA oxidation (Fig. S16a). Acetone is used to dissolve β -carotene, and the solvent effects of acetone on SMX degradation could be ignored (Fig. S16b). As observed in Fig. 4f and Fig. S16c, the oxidation of SMX was significantly inhibited in the presence of β -carotene (1.0–10 mM), evidencing the significant role of singlet oxygenation for SMX degradation. On the other hand, the possible role of other non-radical pathways such as the generation of Cu(III) and the mediated electron transfer process could be excluded in the $\text{Cu}_{\text{SA}}\text{-N-C/PAA}$ process (Fig. S17, S18, Text S4). Overall, the results presented above provide strong evidences that $^1\text{O}_2$ was the primary reactive species responsible for SMX degradation, while $\text{HO}_2^{\bullet}/\text{O}_2^{\bullet-}$ might serve as the intermediates for $^1\text{O}_2$ generation.

3.3.2. Generation mechanism of $^1\text{O}_2$ in the $\text{Cu}_{\text{SA}}\text{-N-C/PAA}$ system

It was reported that $^1\text{O}_2$ could be generated via the reactions of $\text{HO}_2^{\bullet}/$

$\text{O}_2^{\bullet-}$ with $\bullet\text{OH}$ and H^+ (Eqs. 5 and 6) [45]. The EPR signal of $^1\text{O}_2$ was obviously decreased after addition of $p\text{-BQ}$ as a scavenger of $\text{HO}_2^{\bullet}/\text{O}_2^{\bullet-}$ (Fig. 4g), while the degradation of SMX was also suppressed (Fig. 4d). These results also supported that $\text{HO}_2^{\bullet}/\text{O}_2^{\bullet-}$ should behave as an intermediate for $^1\text{O}_2$ generation. Besides, the intensity of $\text{TEMP-}^1\text{O}_2$ adduct (Fig. 4h) as well as the $\text{DMPO-HO}_2^{\bullet}/\text{O}_2^{\bullet-}$ adduct (Fig. 4i) in the $\text{Cu}_{\text{SA}}\text{-N-C/PAA}$ system decreased after excluding oxygen. This finding suggests that dissolved oxygen in the water could contribute to the production of $^1\text{O}_2$ by generating $\text{HO}_2^{\bullet}/\text{O}_2^{\bullet-}$ as intermediates (Fig. S19, S20, details discussed in Text S5).



DFT calculations were performed to probe the underlying mechanism of $^1\text{O}_2$ generation from PAA on CuN_4 sites. The results show that PAA prefers to bind to the Cu-pyridine N_4 site via the single O atom in the C-O bond, and then divides into OH^* and CH_3COO^* moieties spontaneously (Fig. S21a) to facilitate the generation of $^1\text{O}_2$. CH_3COO^* was finally released exothermically as CH_3COOH . The energy change

plot for different steps illustrated a decrease in relative energy for the adsorption of PAA on CuN₄ site (Fig. S21b), implying that the stable adsorption of PAA by CuN₄ site could be realized spontaneously via the form of CH₃COO-CuN₄ bond. Subsequently, the following reaction for generating ¹O₂ is initiated with OH* moiety further absorbed and transformed on the Cu-pyridine N₄ site (Fig. S32a). To be specific, OH* firstly absorbs onto the Cu-pyridine N₄ site, followed by the loss of H from *OH to form *O, and then the direct desorption of O generates ¹O₂ (OH* → *O → ¹O₂, denoted as path I, Fig. 5a). The abovementioned results proved that HO₂*/O₂* was a significant source of ¹O₂ in the Cu_{SA}-N-C/PAA process and thus, another path to produce ¹O₂ from OOH* is proposed. As shown in Fig. 5b, the adsorption of OOH* occurred on the CuN₄ site and O₂* moiety is formed after the desorption of H, followed by the generation of ¹O₂ (OOH* → O₂* → ¹O₂, denoted as path II). The Gibbs free energy of the two potential pathways for ¹O₂ production on the CuN₄ site are shown in Figs. 5c and 5d. The total energy released during the reaction are 1.53 eV and 1.37 eV for path I and path II, respectively, indicating that the production of ¹O₂ from *OH and OOH* on CuN₄ site are thermodynamically favorable.

3.4. Origin of high activity of Cu-N₄ configuration in PAA activation

The single-atomic Cu sites on nitrogen-doped carbon nanosheets displays an excellent performance on PAA activation. DFT calculations were performed to gain a deeper understanding of the underlying mechanism. Four simulated configurations including N-doped carbon nanosheets, CuC₄, CuN₂C₂ and CuN₄ are depicted in Fig. S22, and the optimized adsorption structures of the PAA molecule on different configurations are shown in Fig. S23 with corresponding adsorption energies (*E*_{ads}) and average O–O bond lengths (*l*_{O–O}) provided in Table S7.

The *E*_{ads} of PAA onto the different structure models followed the sequence: N-doped carbon nanosheets (-1.397 eV) > CuC₄ (-1.593 eV) > CuN₂C₂ (-2.586 eV) > CuN₄ (-2.752 eV). The results reflected the strong affinity of isolated Cu–N sites towards the PAA molecule. Additionally, the *l*_{O–O} of PAA molecule was stretched after adsorption, which was elongated from 1.490 Å in free PAA to 1.492, 1.518, 1.563 and 1.576 Å on N-doped carbon nanosheets, CuC₄, CuN₂C₂ and CuN₄ models, respectively. The results indicated the higher catalytic activity of single-atomic Cu–N sites on PAA activation over the N/C sites. Moreover, the PAA adsorption energy and the O–O bond stretching on CuN₄ were larger than those of other configurations, revealing that CuN₄ configuration possessed higher activity on PAA adsorption and activation. To further support this finding, the partial density of states (PDOS) of Cu atom in the CuC₄, CuN₂C₂ and CuN₄ configurations were calculated and shown in Fig. 5a. Obviously, the distribution of bonding orbital (mostly above the Fermi level) in the Cu 3d orbital was effectively optimized via N coordination. The 3d orbital electrons of a Cu atom in nitrogen-free CuC₄ located at 1.96 eV above the Fermi level, while those of Cu atoms in CuN₂C₂ and CuN₄ shifted closer to the Fermi level at 0.39 and 0.07 eV, respectively. The closer Fermi-level electrons means that the catalytic activities of CuN₂C₂ and CuN₄ in PAA activation are much stronger than that of CuC₄ without N allocation [46].

The two-dimensional charge distribution of the Cu-pyridinic N₄ model was further obtained and shown in Fig. 5b. The charge density follows the order: single Cu atom > pyridinic N > C atoms bonded to pyridinic N and this phenomenon is ascribed to the difference of Cu, N and C atoms in valence electrons and electronegativity [47]. The Bader charge of the isolated Cu atom is also significantly higher than that of eight C atoms adjacent to pyridinic N (labelled C1 to C8 in Fig. 5c) (Fig. 5d). Hence, the single Cu atom and eight C atoms respectively

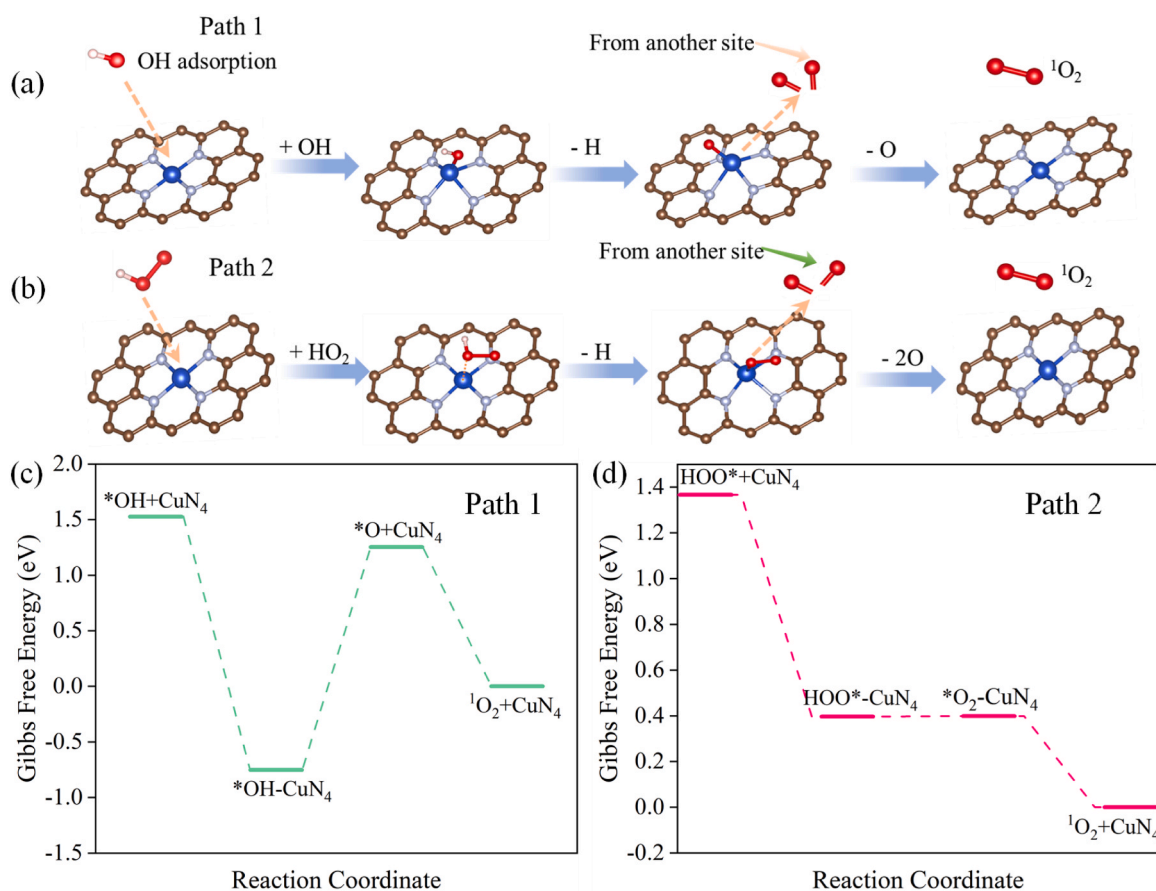


Fig. 5. Schematic diagram of the reaction pathways for ¹O₂ production on Cu-N₄ site from (a) *OH (Path 1) and (b) *HO₂ (Path 2) (Grey for C, red for O, silver for N, white for H and blue for Cu). (c) and (b) Gibbs free energy calculation of the two pathways for ¹O₂ formation.

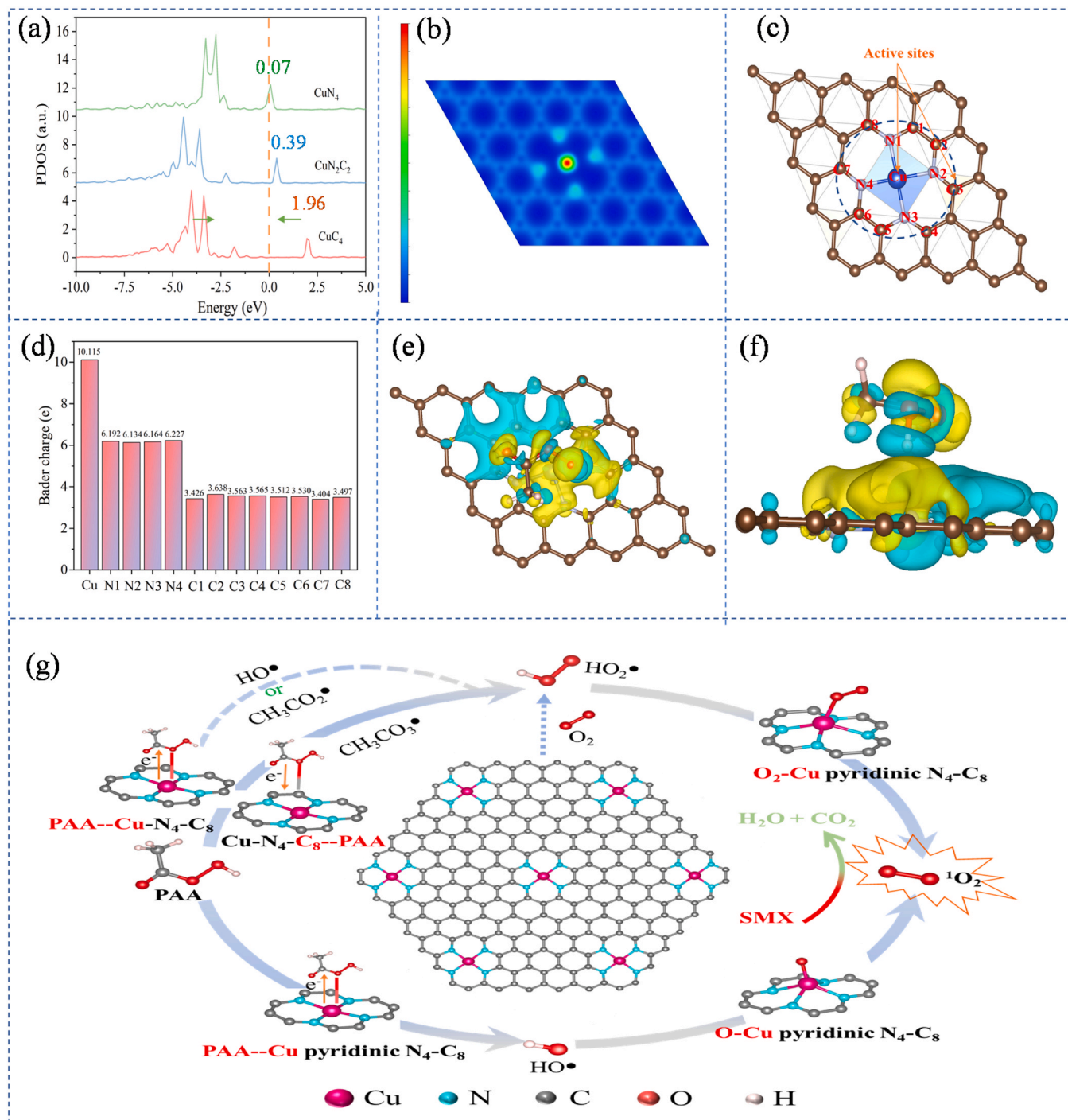


Fig. 6. (a) The partial density of states (PDOS) of Cu-pyridinic N₄, Cu-pyrrole N₂ and Cu-C₄ configuration; (b) charge distribution image for the Cu-pyridinic N₄ configuration; (c) schematic model of the active sites in the Cu_{SA}-N-C, including a Cu atom and eight C atoms adjoining to pyridinic N; calculated charge density difference of PAA adsorbed on Cu_{SA}-N-C: (d) top view and (e) side view; (f) bader charges of single-atom Cu, pyridinic N and eight C atoms attached to pyridinic N. (g) Proposed mechanism behind PAA activation over the Cu_{SA}-N-C toward SMX oxidation.

served as the electron-rich and electron-poor sites in Cu_{SA}-N-C due to the charge redistribution. Experiments were further conducted to investigate the active sites of Cu_{SA}-N-C for PAA activation. As shown in Fig. S24, the degradation of SMX was significantly enhanced by the increasing copper loading of Cu_{SA}-N-C, suggesting the significant role of copper sites in PAA activation. Noted that oxalic acid has a strong affinity to copper and can deactivate the isolated copper center in catalytic reactions [48]. As Fig. S25a shows, the addition of oxalic acid significantly hindered the degradation of SMX by PAA with the activation of

Cu_{SA}-N-C, while oxalic acid was resistant to the oxidation of the Cu_{SA}-N-C/PAA process (Fig. S25b), indicating that the single Cu atoms behave as the active sites for PAA activation. The XPS analysis revealed that single atomic Cu in Cu_{SA}-N-C are composed of Cu(II) and Cu(I) with a ratio of 0.55: 0.45 (Fig. S4b). Cu(I) was reported to exhibit a stronger activity on PAA activation than Cu(II) [18]. Indeed, the addition of neocuproine, a chelator of Cu(I), dramatically suppressed the oxidation of SMX in the Cu_{SA}-N-C/PAA process (Fig. S26), indicating Cu(I) as the dominant active center to activate PAA.

We further performed DFT calculations to investigate the adhesion of PAA to the catalytic site of Cu_{SA}-N-C and the subsequent mutual electron exchange process. Two representative electron-deficient C atoms, i.e., C2 and C7 with the highest and lowest Bader charge, respectively, are selected as the active sites toward PAA. The Bader charges of Cu atom, C2 and C7 sites underwent noticeable variations after interacting with PAA (Table S8). More specifically, the single-atom Cu loses 0.062e of Bader charge upon adhesion to PAA, suggesting the electron transfer from the electron-rich Cu sites to PAA. On the other hand, the increase in Bader charges of the electron-poor C2 and C7 sites were observed after PAA adsorption (Table S9), which reflected the electron transfer from PAA to the electron-poor C2 and C7 sites.[47] This process will induce the oxidation of PAA to generate CH₃COOO• (Eq. 2), which could be further converted to ¹O₂. This result indicated that the electron-deficient C atoms connecting four pyridinic N atoms can also serve as the active site for PAA. Moreover, the charge density analysis clearly verified the strong electron transfer between the PAA molecule and single-atom Cu, as well as the electron-deficient C sites adjacent to pyridinic N (Figs. 5e and 5f). Combining the experimental results and DFT calculations, the configuration of Cu-pyridinic N₄ in Cu_{SA}-N-C can create a double engine for PAA activation, i.e., the electron-rich Cu single atom and eight electron-poor C atoms neighboring pyridinic N. Such a phenomenon enables a considerable increase in active sites and thus strongly stimulates the electron transfer between the PAA molecule and Cu_{SA}-N-C. Fig. 5g displays a diagram illustrating the proposed catalytic mechanisms for the Cu_{SA}-N-C/PAA system.

3.5. Degradation products and toxicity evolution of SMX

Five major TPs (TP 299, TP 283, TP 254, TP 230 and TP 114) were identified (Fig. S27) and the possible degradation pathways of SMX were proposed in Fig. S28. Highest occupied molecular orbital (HOMO) analysis showed that the aromatic aniline moiety of SMX possesses a higher charge density (Fig. S29), suggesting that the electrophilic attack would preferentially occur on the aromatic amine. The oxidation of aromatic amine (–NH₂) by ¹O₂ generated nitroso-SMX as an intermediate product, which can be further oxidized to nitro-SMX (TP283) and hydroxylated nitro-SMX (TP299) (pathway I). Subsequently, the cleavage of the S–N bond in TP299 produced TP114. Furthermore, the aromatic amine can also be substituted by hydroxyl to generate TP254, followed by the attack on isoxazole ring producing TP230 (pathway II). More importantly, the direct hydroxylated SMX (SMX-OH) was always the primary transformation product in SMX oxidation by •OH or R–O• [38,49–51]. Besides, the coupling reaction between the formed N-centered radicals from SMX and SMX-OH was generally reported as an important process in the radical-based AOPs [52,53]. However, SMX-OH and the dimeric products were not detected in the Cu_{SA}-N-C/PAA system, further confirming the negligible role of •OH and R–O• in SMX oxidation. The biotoxicity of aqueous solution containing SMX was obviously lowered after degradation based on the analysis of ecological structure activity relationship (ECOSAR) program (Table S10, Table S11, Text S6).

3.6. Applications of the Cu_{SA}-N-C/PAA process in actual waters

The effects of common water matrices on SMX degradation in the Cu_{SA}-N-C/PAA system are evaluated. As Fig. S30a shows, the degradation of SMX was slightly inhibited after addition of 1.0–5.0 mg L^{−1} humic acid (HA). As widely reported, however, HA can cause serious suppression on the conventional radical-driven PAA-based AOPs. For example, HA was reported to severely inhibit SMX and naproxen degradation in Co/PAA process and UV/PAA process, respectively, owing to the rapid reaction between HA and the radical species (i.e., •OH and R–O•, $k_{R-O\bullet}$ or $k_{OH/HA} = 10^4 \text{ L mg}^{-1} \text{ s}^{-1}$) [19,38]. Hence, the slight inhibition of HA implied that the primary reactive species in the Cu_{SA}-N-C/PAA system might be different from the conventional

PAA-based AOPs. Also, the Cu_{SA}-N-C/PAA system exhibited high tolerance towards the common inorganic ions. The oxidation of SMX was slightly affected by Cl[−] (Fig. S30b) and CO₃^{2−}/HCO₃[−] (Fig. S30c), and not influenced by NO₃[−] (2.0 mM), Ca²⁺ (5.0 mg L^{−1}) and Mg²⁺ (5.0 mg L^{−1}) (Fig. S30d). The sudden increase of SMX removal with Cl[−] elevated to 500 mM might be attributed to the generation of HClO [54]. Noting that CO₃^{2−}/HCO₃[−] can cause serious inhibition to the conventional metal-activated PAA systems due to quenching of radical species (•OH and R–O•) [18,55]. The negligible impact of CO₃^{2−}/HCO₃[−] further implied that the Cu_{SA}-N-C/PAA process might not proceed via radical process, which will be comprehensively unveiled in the following section. Then, SMX degradation by Cu_{SA}-N-C/PAA process was also examined in the real water samples. The degradation of SMX was virtually unaffected in the surface water, and merely slightly decreased in the wastewater (Fig. S31). Hence, the Cu_{SA}-N-C/PAA process can achieve highly selective removal of SMX from complicated water matrices.

4. Conclusion

This work is among the first report aimed at applying atomically dispersed Cu activators (Cu_{SA}-N-C) to boost the PAA activation for wastewater decontamination. The activation of PAA with Cu_{SA}-N-C possesses several significant merits, which enables it highly promising to selectively remove target organic pollutants from wastewater. The Cu_{SA}-N-C exhibits superior catalytic activity and robust stability towards PAA activation, and the amount of copper ions leached from Cu_{SA}-N-C is quite limited during the consecutive cycles. More interestingly, singlet oxygen (¹O₂) rather than radical species was proved to be the dominant oxidizing species in the Cu_{SA}-N-C/PAA system, which is largely different from the conventional PAA-based AOPs. The Cu_{SA}-N-C/PAA system exhibits strong resistance against the typical water matrices with respect to the selective oxidation of specific contaminants. Our mechanistic study unraveled that the remarkable activity of Cu_{SA}-N-C in PAA activation was derived from the ultra-high-density Cu-pyridinic N₄ moieties, which creates not only the electron-rich Cu sites but also the electron-poor C atoms neighboring pyridinic N as the dual catalytic centers. Hence, it is expected to enhance the PAA activation performance of the catalysts by anchoring high-density, well-dispersed metal-N coordination moieties, such as Cu-N_x and Co-N_x sites, on carbon-based substrates with high surface area and conductivity. This work can provide valuable guidance for the optimal design of high-performance PAA activators to achieve efficient wastewater purification.

CRediT authorship contribution statement

Yalei Zhang: Validation, Supervision, Conceptualization. **Ruicheng Ji:** Investigation. **Tongcai Liu:** Methodology. **Yao Xu:** Methodology, Data curation. **Jiabin Chen:** Writing – review & editing, Supervision, Project administration, Funding acquisition, Conceptualization. **Libin Yang:** Investigation. **Xuefei Zhou:** Supervision, Data curation, Conceptualization. **Longlong Zhang:** Writing – original draft, Investigation.

Declaration of Competing Interest

The authors declare that they have no known competing financial interests or personal relationships that could have appeared to influence the work reported in this paper.

Data availability

The data that has been used is confidential.

Acknowledgements

This study was supported by National Natural Science Foundation of China (52122006), Shanghai Science and Technology Innovation Action Plan (No. 22dz1205700), and the Fundamental Research Funds for the Central Universities (No.2022-4-ZD-05).

Appendix A. Supporting information

Supplementary data associated with this article can be found in the online version at doi:10.1016/j.apcatb.2024.123897.

References

- [1] T. Luukkonen, S.O. Pehkonen, Peracids in water treatment: a critical review, *Crit. Rev. Environ. Sci. Technol.* 47 (2017) 1–39.
- [2] X.W. Ao, J. Eloranta, C.H. Huang, D. Santoro, W.J. Sun, Z.D. Lu, C. Li, Peracetic acid-based advanced oxidation processes for decontamination and disinfection of water: a review, *Water Res.* 188 (2020) 116479.
- [3] J. Kim, C.-H. Huang, Reactivity of peracetic acid with organic compounds: a critical review, *ACS EST Water* 1 (2020) 15–33.
- [4] K. Zhang, X. Zhou, P. Du, T. Zhang, M. Cai, P. Sun, C.H. Huang, Oxidation of beta-lactam antibiotics by peracetic acid: reaction kinetics, product and pathway evaluation, *Water Res.* 123 (2017) 153–161.
- [5] P. Du, W. Liu, H. Cao, H. Zhao, C.H. Huang, Oxidation of amino acids by peracetic acid: reaction kinetics, pathways and theoretical calculations, *Water Res.* X 1 (2018) 100002.
- [6] S. Waclawek, H.V. Lutze, K. Gröbel, V.V.T. Padil, M. Černík, D.D. Dionysiou, Chemistry of persulfates in water and wastewater treatment: a review, *Chem. Eng. J.* 330 (2017) 44–62.
- [7] J. Kim, T. Zhang, W. Liu, P. Du, J.T. Dobson, C.H. Huang, Advanced oxidation process with peracetic acid and Fe(II) for contaminant degradation, *Environ. Sci. Technol.* 53 (2019) 13312–13322.
- [8] J. Kim, P. Du, W. Liu, C. Luo, H. Zhao, C.H. Huang, Cobalt/peracetic acid: advanced oxidation of aromatic organic compounds by acetylperoxyl radicals, *Environ. Sci. Technol.* 54 (2020) 5268–5278.
- [9] J. Wu, J. Zou, J. Lin, S. Li, S. Chen, X. Liao, J. Yang, B. Yuan, J. Ma, Hydroxylamine enhanced the degradation of diclofenac in Cu(II)/peracetic acid system: formation and contributions of $\text{CH}_3\text{C}(\text{O})\text{O}\cdot$, $\text{CH}_3\text{C}(\text{O})\text{OO}\cdot$, Cu(III) and $\cdot\text{OH}$, *J. Hazard. Mater.* 460 (2023) 132461.
- [10] S. Correa-Sanchez, G.A. Peñuela, Peracetic acid-based advanced oxidation processes for the degradation of emerging pollutants: a critical review, *J. Water Process Eng.* 49 (2022) 102986.
- [11] L. Zhang, J. Chen, Y. Zhang, Y. Xu, T. Zheng, X. Zhou, Highly efficient activation of peracetic acid by nano-CuO for carbamazepine degradation in wastewater: the significant role of H_2O_2 and evidence of acetylperoxy radical contribution, *Water Res.* 216 (2022) 118322.
- [12] J. Xiao, H. Dong, Y. Li, L. Li, D. Chu, S. Xiang, X. Hou, Q. Dong, S. Xiao, Z. Jin, J. Wang, Graphene shell-encapsulated copper-based nanoparticles (G@Cu-NPs) effectively activate peracetic acid for elimination of sulfamethazine in water under neutral condition, *J. Hazard. Mater.* 441 (2023) 129895.
- [13] Y. Li, K. Li, Q. Wan, X. Xu, R. Cao, J. Wang, T. Huang, G. Wen, Inactivation of fungal spores in water by CuO-activated peracetic acid: kinetics, mechanism and regrowth, *J. Hazard. Mater.* 439 (2022) 129611.
- [14] L. Zhang, Y. Fu, Z. Wang, G. Zhou, R. Zhou, Y. Liu, Removal of diclofenac in water using peracetic acid activated by zero valent copper, *Sep. Purif. Technol.* 276 (2021) 119319.
- [15] Y. Li, K. Li, Q. Wan, X. Xu, R. Cao, J. Wang, T. Huang, G. Wen, Inactivation of fungal spores in water by CuO-activated peracetic acid: kinetics, mechanism and regrowth, *J. Hazard. Mater.* 439 (2022) 129611.
- [16] Z. Yu, J. Wu, J. Zhang, X. Chen, Z. Wang, Y. Zhang, D. Li, J. Chen, H. Liu, P. Chen, W. Lv, G. Liu, Carbon nitride nanotubes anchored with Cu(I) triggers peracetic acid activation with visible light for removal of antibiotic contaminants: probing mechanisms of non-radical pathways and identifying active sites, *J. Hazard. Mater.* 460 (2023) 132401.
- [17] X.-w. Ao, J. Eloranta, C.-H. Huang, D. Santoro, W.-j. Sun, Z.-d. Lu, C. Li, Peracetic acid-based advanced oxidation processes for decontamination and disinfection of water: a review, *Water Res.* 188 (2021) 116479.
- [18] L. Zhang, J. Chen, Y. Zhang, Y. Xu, T. Zheng, X. Zhou, Highly efficient activation of peracetic acid by nano-CuO for carbamazepine degradation in wastewater: the significant role of H_2O_2 and evidence of acetylperoxy radical contribution, *Water Res.* 216 (2022) 118322.
- [19] S. Chen, M. Cai, Y. Liu, L. Zhang, L. Feng, Effects of water matrices on the degradation of naproxen by reactive radicals in the UV/peracetic acid process, *Water Res.* 150 (2019) 153–161.
- [20] Y. Zhao, L. Yu, C. Song, Z. Chen, F. Meng, M. Song, Selective degradation of electron-rich organic pollutants induced by CuO@Biochar: the key role of outer-sphere interaction and singlet oxygen, *Environ. Sci. Technol.* 56 (2022) 10710–10720.
- [21] T. Zhang, A.G. Walsh, J. Yu, P. Zhang, Single-atom alloy catalysts: structural analysis, electronic properties and catalytic activities, *Chem. Soc. Rev.* 50 (2021) 569–588.
- [22] L. Li, X. Chang, X. Lin, Z.J. Zhao, J. Gong, Theoretical insights into single-atom catalysts, *Chem. Soc. Rev.* 49 (2020) 8156–8178.
- [23] Y. Shang, X. Xu, B. Gao, S. Wang, X. Duan, Single-atom catalysis in advanced oxidation processes for environmental remediation, *Chem. Soc. Rev.* 50 (2021) 5281–5322.
- [24] J.H. Kim, D. Shin, J. Lee, D.S. Baek, T.J. Shin, Y.T. Kim, H.Y. Jeong, J.H. Kwak, H. Kim, S.H. Joo, A general strategy to atomically dispersed precious metal catalysts for unravelling their catalytic trends for oxygen reduction reaction, *ACS Nano* 14 (2020) 1990–2001.
- [25] L. Bai, C.S. Hsu, D.T.L. Alexander, H.M. Chen, X. Hu, A. Cobalt-Iron, Double-atom catalyst for the oxygen evolution reaction, *J. Am. Chem. Soc.* 141 (2019) 14190–14199.
- [26] F. Chen, X.-L. Wu, L. Yang, C. Chen, H. Lin, J. Chen, Efficient degradation and mineralization of antibiotics via heterogeneous activation of peroxymonosulfate by using graphene supported single-atom Cu catalyst, *Chem. Eng. J.* 394 (2020) 124904.
- [27] F. Li, Z. Lu, T. Li, P. Zhang, C. Hu, Origin of the excellent activity and selectivity of a single-atom copper catalyst with unsaturated Cu-N₂ sites via peroxydisulfate activation: Cu(III) as a dominant oxidizing species, *Environ. Sci. Technol.* 56 (2022) 8765–8775.
- [28] Z. Lu, P. Zhang, C. Hu, F. Li, Insights into singlet oxygen generation and electron-transfer process induced by a single-atom Cu catalyst with saturated Cu-N₄ sites, *iScience* 25 (2022) 104930.
- [29] C. Lei, Y. Wang, Y. Hou, P. Liu, J. Yang, T. Zhang, X. Zhuang, M. Chen, B. Yang, L. Lei, C. Yuan, M. Qiu, X. Feng, Efficient alkaline hydrogen evolution on atomically dispersed Ni-Nx Species anchored porous carbon with embedded Ni nanoparticles by accelerating water dissociation kinetics, *Energy Environ. Sci.* 12 (2019) 149–156.
- [30] Y. Kan, R. Zhang, X. Xu, B. Wei, Y. Shang, Comparative study of raw and HNO_3 -modified porous carbon from waste printed circuit boards for sulfadiazine adsorption: Experiment and DFT study, *Chin. Chem. Lett.* (2023) 108272.
- [31] Y. Qi, J. Li, Y. Zhang, Q. Cao, Y. Si, Z. Wu, M. Akram, X. Xu, Novel lignin-based single atom catalysts as peroxymonosulfate activator for pollutants degradation: Role of single cobalt and electron transfer pathway, *Appl. Catal. B: Environ.* 286 (2021).
- [32] Chang-Guo Zhan, Jeffrey A. Nichols, D.A. Dixon, Ionization potential, electron affinity, electronegativity, hardness, and electron excitation energy: molecular properties from density functional theory orbital energies, *J. Phys. Chem. A* 107 (2003) 4184–4195.
- [33] P. Hu, H. Su, Z. Chen, C. Yu, Q. Li, B. Zhou, P.J.J. Alvarez, M. Long, Selective degradation of organic pollutants using an efficient metal-free catalyst derived from carbonized polypyrrole via peroxymonosulfate activation, *Environ. Sci. Technol.* 51 (2017) 11288–11296.
- [34] S. Zhu, X. Li, J. Kang, X. Duan, S. Wang, Persulfate activation on crystallographic manganese oxides: mechanism of singlet oxygen evolution for nonradical selective degradation of aqueous contaminants, *Environ. Sci. Technol.* 53 (2018) 307–315.
- [35] T. Ye, Z. Wei, R. Spinney, D.D. Dionysiou, S. Luo, L. Chai, Z. Yang, R. Xiao, Quantitative structure–activity relationship for the apparent rate constants of aromatic contaminants oxidized by ferrate (VI), *Chem. Eng. J.* 317 (2017) 258–266.
- [36] B. Liu, W. Guo, W. Jia, H. Wang, S. Zheng, Q. Si, Q. Zhao, H. Luo, J. Jiang, N. Ren, Insights into the oxidation of organic contaminants by Co(II) activated peracetic acid: The overlooked role of high-valent cobalt-oxo species, *Water Res.* 201 (2021) 117313.
- [37] K. Qian, H. Chen, W. Li, Z. Ao, Y.N. Wu, X. Guan, Single-atom Fe catalyst outperforms its homogeneous counterpart for activating peroxymonosulfate to achieve effective degradation of organic contaminants, *Environ. Sci. Technol.* 55 (2021) 7034–7043.
- [38] Z. Wang, J. Wang, B. Xiong, F. Bai, S. Wang, Y. Wan, L. Zhang, P. Xie, M. R. Wiesner, Application of cobalt/peracetic acid to degrade sulfamethoxazole at neutral condition: efficiency and mechanisms, *Environ. Sci. Technol.* 54 (2020) 464–475.
- [39] M. Cai, P. Sun, L. Zhang, C.-H. Huang, UV/peracetic acid for degradation of pharmaceuticals and reactive species evaluation, *Environ. Sci. Technol.* 51 (2017) 14217–14224.
- [40] Divya Kamath, Mezyk, P. Stephen, Minakate, Daisuke, Elucidating the elementary reaction pathways and kinetics of hydroxyl radical-induced acetone degradation in aqueous phase advanced oxidation processes, *Environ. Sci. Technol.* 52 (2018) 7763–7774.
- [41] J. Kim, P. Du, W. Liu, C. Luo, H. Zhao, C.H. Huang, Cobalt/peracetic acid: advanced oxidation of aromatic organic compounds by acetylperoxyl radicals, *Environ. Sci. Technol.* 54 (2020) 5268–5278.
- [42] J. Fan, H. Qin, S. Jiang, Mn-doped g-C₃N₄ composite to activate peroxymonosulfate for acetaminophen degradation: the role of superoxide anion and singlet oxygen, *Chem. Eng. J.* 359 (2019) 723–732.
- [43] L. Gao, Y. Guo, J. Zhan, G. Yu, Y. Wang, Assessment of the validity of the quenching method for evaluating the role of reactive species in pollutant abatement during the persulfate-based process, *Water Res.* 221 (2022) 118730.
- [44] Shioy Y. Wang, H. Jiao, Scavenging capacity of berry crops on superoxide radicals, hydrogen peroxide, hydroxyl radicals, and singlet oxygen, *J. Agric. Food Chem.* 48 (2000) 5677–5684.
- [45] X. Li, J. Liu, A.I. Rykov, H. Han, C. Jin, X. Liu, J. Wang, Excellent photo-Fenton catalysts of Fe–Co Prussian blue analogues and their reaction mechanism study, *Appl. Catal. B: Environ.* 179 (2015) 196–205.
- [46] X. Zhang, S. Zhang, Y. Yang, L. Wang, Z. Mu, H. Zhu, X. Zhu, H. Xing, H. Xia, B. Huang, J. Li, S. Guo, E. Wang, A general method for transition metal single

- atoms anchored on honeycomb-like nitrogen-doped carbon nanosheets, *Adv. Mater.* 32 (2020) e1906905.
- [47] Y. Gao, Y. Zhu, T. Li, Z. Chen, Q. Jiang, Z. Zhao, X. Liang, C. Hu, Unraveling the high-activity origin of single-atom iron catalysts for organic pollutant oxidation via peroxymonosulfate activation, *Environ. Sci. Technol.* 55 (2021) 8318–8328.
- [48] L.V. Perelomov, D.L. Pinskiy, A. Violante, Effect of organic acids on the adsorption of copper, lead, and zinc by goethite, *Eurasia Soil Sci.* 44 (2011) 22–28.
- [49] J. Wang, Y. Wan, J. Ding, Z. Wang, J. Ma, P. Xie, M.R. Wiesner, Thermal activation of peracetic acid in aquatic solution: the mechanism and application to degrade sulfamethoxazole, *Environ. Sci. Technol.* 54 (2020) 14635–14645.
- [50] Amina, X. Si, K. Wu, Y. Si, B. Yousaf, Mechanistic insights into the reactive radicals-assisted degradation of sulfamethoxazole via calcium peroxide activation by manganese-incorporated iron oxide-graphene nanocomposite: formation of radicals and degradation pathway, *Chem. Eng. J.* 384 (2020) 123360.
- [51] S.G. Michael, I. Michael-Kordatou, S. Nahim-Granados, M.I. Polo-López, J. Rocha, A.B. Martínez-Piarnas, P. Fernández-Ibáñez, A. Agüera, C.M. Manaia, D. Fatta-Kassinos, Investigating the impact of UV-C/H₂O₂ and sunlight/H₂O₂ on the removal of antibiotics, antibiotic resistance determinants and toxicity present in urban wastewater, *Chem. Eng. J.* 388 (2020) 124383.
- [52] C. Dai, S. Li, Y. Duan, K.H. Leong, S. Liu, Y. Zhang, L. Zhou, Y. Tu, Mechanisms and product toxicity of activated carbon/peracetic acid for degradation of sulfamethoxazole: implications for groundwater remediation, *Water Res.* 216 (2022) 118347.
- [53] J. Wang, B. Xiong, L. Miao, S. Wang, P. Xie, Z. Wang, J. Ma, Applying a novel advanced oxidation process of activated peracetic acid by CoFe₂O₄ to efficiently degrade sulfamethoxazole, *Appl. Catal. B: Environ.* 280 (2021) 119422.
- [54] L. Zhang, J. Chen, T. Zheng, Y. Xu, T. Liu, W. Yin, Y. Zhang, X. Zhou, Co–Mn spinel oxides trigger peracetic acid activation for ultrafast degradation of sulfonamide antibiotics: Unveiling critical role of Mn species in boosting Co activity, *Water Res.* 229 (2023) 119462.
- [55] R. Ji, J. Chen, T. Liu, X. Zhou, Y. Zhang, Critical review of perovskites-based advanced oxidation processes for wastewater treatment: operational parameters, reaction mechanisms, and prospects, *Chin. Chem. Lett.* 33 (2022) 643–652.